

Magma fragmentation in highly explosive basaltic eruptions induced by rapid crystallization

Arzilli, Fabio; La Spina, Giuseppe; Burton, Mike R.; Polacci, Margherita; Le Gall, Nolwenn; Hartley, Margaret E.; Di Genova, Danilo; Cai, Biao; Vo, Nghia T.; Bamber, Emily C.; Nonni, Sara; Atwood, Robert; Llewellyn, Edward W.; Brooker, Richard A.; Mader, Heidi M.; Lee, Peter D.

DOI:

[10.1038/s41561-019-0468-6](https://doi.org/10.1038/s41561-019-0468-6)

License:

Other (please specify with Rights Statement)

Document Version

Peer reviewed version

Citation for published version (Harvard):

Arzilli, F, La Spina, G, Burton, MR, Polacci, M, Le Gall, N, Hartley, ME, Di Genova, D, Cai, B, Vo, NT, Bamber, EC, Nonni, S, Atwood, R, Llewellyn, EW, Brooker, RA, Mader, HM & Lee, PD 2019, 'Magma fragmentation in highly explosive basaltic eruptions induced by rapid crystallization', *Nature Geoscience*, vol. 12, no. 12, pp. 1023-1028. <https://doi.org/10.1038/s41561-019-0468-6>

[Link to publication on Research at Birmingham portal](#)

Publisher Rights Statement:

Checked for eligibility: 05/11/2019

This document is the Author Accepted Manuscript version of a published work, Arzilli, F., Spina, G., Burton, M.R. et al. Magma fragmentation in highly explosive basaltic eruptions induced by rapid crystallization. *Nat. Geosci.* (2019) doi:10.1038/s41561-019-0468-6, which appears in its final form at: <https://doi.org/10.1038/s41561-019-0468-6>

Subject to Springer Nature reuse terms: <https://www.nature.com/nature-research/editorial-policies/self-archiving-and-license-to-publish#terms-for-use>

General rights

Unless a licence is specified above, all rights (including copyright and moral rights) in this document are retained by the authors and/or the copyright holders. The express permission of the copyright holder must be obtained for any use of this material other than for purposes permitted by law.

- Users may freely distribute the URL that is used to identify this publication.
- Users may download and/or print one copy of the publication from the University of Birmingham research portal for the purpose of private study or non-commercial research.
- User may use extracts from the document in line with the concept of 'fair dealing' under the Copyright, Designs and Patents Act 1988 (?)
- Users may not further distribute the material nor use it for the purposes of commercial gain.

Where a licence is displayed above, please note the terms and conditions of the licence govern your use of this document.

When citing, please reference the published version.

Take down policy

While the University of Birmingham exercises care and attention in making items available there are rare occasions when an item has been uploaded in error or has been deemed to be commercially or otherwise sensitive.

If you believe that this is the case for this document, please contact UBIRA@lists.bham.ac.uk providing details and we will remove access to the work immediately and investigate.

1 **Magma fragmentation in highly explosive basaltic eruptions induced by rapid crystallisation**

2

3 Fabio Arzilli¹, Giuseppe La Spina¹, Mike R. Burton¹, Margherita Polacci¹, Nolwenn Le Gall²,
4 Margaret E. Hartley¹, Danilo Di Genova³, Biao Cai⁴, Nghia T. Vo⁵, Emily C. Bamber¹, Sara
5 Nonni⁵, Robert Atwood⁵, Ed W. Llewelin⁶, Richard A. Brooker⁷, Heidy Mader⁷ and Peter D. Lee²

6

7 ¹School of Earth and Environmental Sciences, University of Manchester, Manchester M139PL, UK

8 ²Department of Mechanical Engineering, University College London, London, UK

9 ³Institute of Non-Metallic Materials, Clausthal University of Technology, Zehntner Str. 2a, 38678

10 Clausthal-Zellerfeld, Germany

11 ⁴ School of Metallurgy and Materials, University of Birmingham, Birmingham B15 2TT, UK

12 ⁵Diamond Light Source, Harwell Science and Innovation Campus, Didcot OX11 0DE, UK

13 ⁶Department of Earth Sciences, Durham University, Durham DH1 3LE, UK

14 ⁷School of Earth Sciences, University of Bristol, Bristol BS8 1RJ, UK

15

16

17 *Corresponding author: Dr. Fabio Arzilli

18 Corresponding author present affiliation: School of Earth and Environmental Sciences, The

19 University of Manchester, Oxford Road, Manchester, M13 9PL, UK

20 E-mail address: fabio.arzilli@manchester.ac.uk

21 Phone: +393298429732; +447904104670

22

23

24 **Basaltic eruptions are the most common form of volcanism on Earth and planetary bodies.**
25 **The low viscosity of basaltic magmas inhibits fragmentation, favouring effusive and lava-**
26 **fountaining activity, yet highly explosive, hazardous basaltic eruptions do occur. The**
27 **processes that promote fragmentation of basaltic magma remain unclear, and are subject to**
28 **debate. Here, we use a numerical conduit model to show that rapid ascent of magma during**
29 **explosive eruption produces large undercooling. Novel *in situ* experiments reveal that**
30 **undercooling drives exceptionally rapid (~minutes) crystallisation, inducing a step-change in**
31 **viscosity that triggers magma fragmentation. Experimentally-produced textures are**
32 **consistent with products of basaltic Plinian eruptions. We apply the numerical model to**
33 **investigate basaltic magma fragmentation over a wide parameter space and find that all**
34 **basaltic volcanoes have the potential to produce highly explosive eruptions. The critical**
35 **requirements are initial magma temperatures lower than 1100 °C, in order to reach a syn-**
36 **eruptive crystal content of > 30 vol.%, and thus a magma viscosity $\geq 10^5$ Pa s, which our**
37 **results suggest is the minimum viscosity required for the fragmentation of fast ascending**
38 **basaltic magmas. Our study provides both a demonstration and explanation of the processes**
39 **that drive basaltic Plinian eruptions, revealing how typically effusive basaltic volcanoes can**
40 **produce unexpected highly explosive, and hazardous, eruptions.**

41

42 Explosive eruptions are undoubtedly the most violent and catastrophic expression of volcanic
43 activity^{1,2}. Highly explosive Plinian eruptions can inject $> 0.1 \text{ km}^3$ of pyroclastic material producing
44 volcanic plumes that can reach up to 40 km in height, impacting both regional and global climate,
45 and producing a significant threat to proximal populations^{3,4}. Basaltic volcanoes are usually
46 characterised by effusive and mild-explosive lava fountaining activity⁵, however, basaltic Plinian
47 eruptions can occur⁶⁻¹¹. The main process characterising highly explosive activity is magma
48 fragmentation, which is the transition from ductile to brittle behaviour of molten magma^{1,2}. For
49 silicic magmas, fragmentation is attributed to high strain rates associated with acceleration of the
50 bubbly mixture^{1,12-14} or from the bubble overpressure associated with restricted bubble
51 expansion^{14,15-18}. The low viscosity of basaltic magmas, however, makes high strain rates, or the
52 bubble overpressure necessary to trigger fragmentation difficult to achieve^{1,19}.

53 Crystallisation during magma ascent may significantly increase magma viscosity, leading to
54 fragmentation²⁰. However, crystallisation in basaltic magmas has previously been thought to occur
55 on timescales significantly longer than the time required for magma to ascend from a crustal storage
56 chamber to the vent²¹, particularly in the case of highly explosive eruptions.

57 In volcanic conduits, the crystallisation kinetics of an ascending magma are driven by degassing
58 and cooling²²⁻²³. Plagioclase and pyroxene crystallisation are sensitive indicators of magma
59 dynamics in volcanic conduits^{21,24-27} and their kinetically controlled abundance can rapidly change
60 magma rheology²⁸⁻²⁹. Our understanding of crystallisation kinetics in magmas is underpinned by *ex*
61 *situ* crystallisation quench experiments. Here we perform novel *in situ* experiments in order to
62 visualize and quantify the evolution of rapid crystallisation in basaltic magmas, as with this
63 approach it is possible to ascertain in real time when crystals start to form and how quickly magma
64 crystallinity evolves.

65 A frequently used model to describe crystallisation as function of time is given by an exponential
66 law^{21,23}, where the rate of crystallisation is controlled by the characteristic time $\tau^{(c)}$. The
67 characteristic time is a measure of how fast a process will approach the equilibrium^{21,30}. The smaller

68 $\tau^{(c)}$, the faster crystals reach their equilibrium abundance (see Methods section). La Spina et al. (ref.
69 21) demonstrated that the time required to reach the equilibrium crystal fraction in basalts is ~ 4.6
70 times $\tau^{(c)}$. Furthermore, during mild lava-fountaining basaltic activity²¹, $\tau^{(c)}$ is in the order of
71 thousands seconds, resulting in a crystallisation time of ~ 2 hours. Crystallisation rate increases with
72 magma ascent rate, as cooling and decompression rates increase³⁰⁻³⁴. Therefore, $\tau^{(c)}$ is smaller and
73 the equilibrium crystal fraction will be reached faster. However, the characteristic times of crystal
74 growth during fast magma ascent have not been quantified.

75 In order to quantify the characteristic times of plagioclase and pyroxene crystallisation during
76 rapid ascent of basaltic magma, here we present the first *in situ* 4D (3D plus time) crystallisation
77 kinetics experiments under fast cooling rates, using fast synchrotron X-ray microtomography. Our
78 experiments provide the first estimation of the characteristic time for plagioclase and pyroxene
79 crystallisation in trachybasaltic magmas during a rapid and continuous increase of undercooling,
80 where ΔT is defined as the difference between the highest temperature at which plagioclase and
81 pyroxene is expected to crystallise and the temperature of the magma²⁴⁻²⁷.

82

83 **Crystallisation experiments at high undercooling**

84 Crystallisation experiments were performed *in situ* at beamline I12-JEEP, Diamond Light
85 Source, Harwell, UK, using a trachybasaltic glass (Supplementary Table 1) from the 2001 Etna
86 eruption as the starting material (see Methods). We combined a bespoke high-temperature
87 environmental cell³⁵ with fast synchrotron X-ray microtomography to image the evolution of
88 crystallisation in real time³⁶ in two experiments. In the first part of the experiment, crystallisation
89 was induced by decreasing temperature from 1250 °C to either 1170 °C or 1150 °C at 0.4 °C s⁻¹ at
90 ambient pressure with a dwell time at the final temperature of 4 h³⁶ (Supplementary Fig. 1). During
91 these 4 h, blocky and prismatic clinopyroxene and oxide crystals were able to grow³⁶ (Fig. 1 and
92 Supplementary Figs. 2 and 3), and the residual melt evolved to a basaltic trachyandesitic
93 composition (Supplementary Table 1; Supplementary Figs. 2 and 3). After 4 h at sub-liquidus

94 conditions (1170 °C and 1150 °C), the system was perturbed through a rapid cooling rate of 0.4 °C
95 s⁻¹, inducing a sudden and continuous increase of undercooling (ΔT). This produced a rapid
96 crystallisation event from the residual melt (Fig. 1; Supplementary Figs. 2 and 3). Our results show
97 that skeletal plagioclase crystals grew during this final stage of rapid cooling, specifically between
98 1112 and 1073 °C after a dwell time of 4 hours at 1150 °C (Fig. 1) and between 1131 and 1053 °C
99 after a dwell time of 4 hours at 1170 °C (Supplementary Fig. 3a,b,c). Plagioclase crystals grew to
100 equilibrium abundance in ~100 seconds (Fig.1), i.e. between two 3D scans. Following this initial
101 burst of rapid plagioclase growth, dendritic clinopyroxene crystals began to nucleate
102 heterogeneously on plagioclase and grew to their final size in the following 180 seconds (Fig. 1b,c;
103 Supplementary Figs. 2b,c, 3d,e, 4 and 5).

104 The large ΔT reached in a relatively short time during our *in situ* 4D crystallisation experiments
105 generated distinctive skeletal plagioclase crystals with swallow-tail morphology and dendritic
106 pyroxene (Fig. 2a-c), similar to the skeletal plagioclase and dendritic pyroxene crystals observed in
107 the products of explosive basaltic Plinian eruptions^{7-11,37,38}, such as Etna 122 B.C.^{7,8,37,38} (Fig. 2d).
108 Heterogeneous nucleation of dendritic pyroxene on skeletal plagioclase (Fig. 1b) is observed to
109 occur in ~180 s during our 4D experiments. These distinctive textures are also reported in products
110 of the Fontana Lapilli (Nicaragua)^{11,37,38} and 1886 Tarawera (New Zealand) eruptions^{7,9,10}.
111 Therefore, all the studied examples of basaltic Plinian deposits show features that are consistent
112 with the textures produced in our experiments. Furthermore, the signature skeletal and dendritic
113 pyroxene is also observed in sub-Plinian eruption (Yufune 2) products of Mt. Fuji (Japan)³⁹.

114 Skeletal plagioclase crystallisation occurred at ΔT between 60 and 140 °C with a growth rate of
115 3×10^{-5} cm s⁻¹ (mm h⁻¹) (Supplementary Table 2), whilst dendritic pyroxene crystallised at ΔT
116 between 60 and 175 °C with a growth rate of 2×10^{-5} cm s⁻¹ (mm h⁻¹) (Supplementary Table 2). This
117 indicates that a rapid increase of ΔT (>60 °C) induces fast crystallisation. As the equilibrium
118 pyroxene crystal content is achieved within ~180 s, we can infer that the pyroxene characteristic
119 time under large ΔT is < 40 s. For plagioclase, where the equilibrium crystal content is achieved

120 within 90 s the characteristic time is < 20 s. These are about two orders of magnitude less than the
121 characteristic time found by La Spina et al. (ref. 21) for effusive and mild lava fountaining activity
122 at Etna (Italy), Stromboli (Italy) and Kilauea (Hawaii), which involved much smaller ΔT (30-60
123 $^{\circ}\text{C}$)²¹ and magma ascent rates of ~ 3 m s⁻¹.

124 *Ex situ* experiments were also performed using a TZM cold seal pressure vessel apparatus, in
125 order to investigate whether fast crystallisation also occurs in a hydrous trachybasaltic melt during
126 rapid and continuous cooling and decompression (see Methods), simulating fast magma ascent in
127 the conduit. The experimental approach consisted of holding the sample for 30 minutes at 75 MPa
128 and 1070 $^{\circ}\text{C}$ before the sample was decompressed and the temperature decreased. After 30 minutes
129 pressure and temperature were decreased continuously for 300 s at 0.2 MPa s⁻¹ and 0.2 $^{\circ}\text{C}$ s⁻¹
130 respectively, reaching 15 MPa and 1010 $^{\circ}\text{C}$ (Supplementary Table 3; Supplementary Fig. 6). The
131 rapid decompression and cooling enabled large ΔT s to be achieved (>100 $^{\circ}\text{C}$; see
132 Supplementary Fig. 6) in 300 s, favouring predominantly clinopyroxene crystallisation, with minor
133 plagioclase and oxide (Supplementary Fig. 7). This indicates that $\tau^{(c)}$ is < 60 s, in agreement with
134 the order of magnitude estimated from *in situ* experiments.

135 Large undercooling can produce significant syn-eruptive microlite crystallisation during rapid
136 magma ascent²⁴⁻²⁷. This increase in crystallinity dramatically increases the viscosity of the
137 magma¹⁹. This process has been proposed to explain explosive basaltic Plinian eruptions, supported
138 by evidence of high microlite contents^{7-11,37,38}. However, a mechanism for this exceptionally fast
139 crystallisation during rapid magma ascent in basaltic Plinian eruptions, favouring fragmentation,
140 has not been demonstrated so far.

141

142 **Numerical simulation of the 122 B.C. Etna basaltic Plinian eruption**

143 Magma fragmentation in basaltic Plinian eruptions has been investigated with conduit models,
144 where crystallisation has been assumed either to be constant²⁰ or at equilibrium⁴⁰. Recent results
145 demonstrate that disequilibrium crystallisation plays a fundamental role in magma dynamics within

146 the conduit²¹, but syn-eruptive disequilibrium crystallisation has not yet been considered for basaltic
147 explosive volcanism^{20,40}.

148 We used the conduit model described by La Spina et al. (ref. 21, 23) to investigate the effect of
149 the new experimentally constrained characteristic times for crystallisation with large undercooling
150 derived here on the ductile-brittle transition of basaltic magma during highly explosive eruptions.
151 Since we are focussing our attention on explosive eruptions with high mass eruption rates ($>10^6$
152 kg/s), it is reasonable to assume that outgassing is negligible for this kind of activity. Indeed,
153 outgassing will be inhibited by fast magma ascent and fragmentation will be achieved faster than
154 outgassing⁴¹. As a test case, we consider the 122 B.C. Etna basaltic Plinian eruption⁶⁻⁸. To model
155 fragmentation we adopt the strain-rate criterion introduced by Papale (ref. 1):

$$156 \quad \dot{\gamma} = k \frac{G_{\infty}}{\mu} \quad (1)$$

157 where $\dot{\gamma}$ is the elongational strain rate, $k=0.01$ is a constant, μ is the magmatic viscosity and G_{∞}
158 is the elastic modulus at infinite frequency. The other constitutive equations are reported in the
159 Methods section. In Figure 3 we report the calculated plagioclase undercooling, crystal content and
160 viscosity as function of depth for $\tau^{(c)} = 10$ and 1000 s. Large undercooling is produced by adiabatic
161 expansion of exsolved volatiles, and mitigated by the latent heat of crystallisation for $\tau^{(c)} = 10$ s
162 (Fig. 3a). In this case, numerical results show a rapid increase in crystallinity and in viscosity at
163 depths below 2 km (Fig. 3c), leading to fragmentation and explosive Plinian eruption. Importantly,
164 numerical results indicate that strain-induced fragmentation is favoured by a combination of rapid
165 viscosity increase (about one order of magnitude in 5 seconds approaching the fragmentation depth)
166 and fast decompression/ascent rates (~ 0.2 MPa s^{-1} and ~ 15 m s^{-1}) that generate high strain rates. For
167 $\tau^{(c)} = 1000$ s, instead, the crystallisation rate is slow, and viscosity stays within the fragmentation
168 threshold all along the conduit.

169

170 **Sensitivity analyses on basaltic magma fragmentation driven by rapid crystallisation**

171 Having established that fast crystallisation plays an important role on basaltic Plinian eruptions,
172 we performed a sensitivity study with our numerical model to investigate the parameter space
173 whereby basaltic fragmentation driven by rapid crystallisation may occur. We use the Etna 122 B.C.
174 eruption as a test case. We focus on the behaviour of ΔT as a function of characteristic time of
175 crystallisation, pressure, temperature and magmatic H₂O content at the conduit inlet, conduit radius,
176 and initial phenocryst content. A detailed description of the initial condition of the sensitivity study
177 can be found in the Methods section. We performed several sensitivity studies assuming a
178 characteristic time of $\tau^{(c)} = 10$ s, as observed in our experiments, and $\tau^{(c)} = 1000$ s, as observed for
179 Etna 2001 in mild explosive activity. We also examined $\tau^{(c)} = 1$ and 100 s for completeness.

180 Numerical results show that undercooling is principally controlled by $\tau^{(c)}$ (Fig. 4a), because the
181 release of latent heat during rapid crystallisation (i.e. small $\tau^{(c)}$) affects the temperature of the
182 system, and, consequently, the undercooling. Therefore, undercooling and characteristic time are
183 linked, affecting one each other. However, our numerical results indicate that, within the parameters
184 space investigated, ΔT is always maintained between 60 and 190 °C (Fig. 4b), which is enough to
185 enable rapid crystallisation in any case. Furthermore, the sensitivity analyses indicate that, after the
186 characteristic time, initial temperature and water content (exsolved + dissolved) play an important
187 role on controlling undercooling (Fig. 4a). ΔT at the point of fragmentation increases as initial
188 temperature decreases (Fig. 4b), meaning that cooler magma in the chamber is more likely to
189 produce microlite crystallisation during ascent, as ΔT will already be large under the pre-eruptive
190 condition. An increase in the initial total H₂O (exsolved + dissolved) also produces an increase of
191 ΔT (Fig. 4c), caused by greater cooling of the system due to enhanced adiabatic gas expansion.
192 Furthermore, higher water content favours rapid crystallisation of microlites, due to the increase in
193 diffusivity within the melt.

194 Our sensitivity studies show that a lower initial temperature and a higher pre-eruptive crystal
195 content results in a greater likelihood of explosive eruptions (Fig. 4d,e). This is consistent with
196 estimates of pre-eruptive temperatures obtained for the Etna and Fontana Plinian eruptions, which

197 range between 1000 and 1060 °C³⁷. Regarding the pre-eruptive crystal content, however, products
198 erupted from basaltic Plinian eruptions are characterized by a small phenocryst content (<10
199 vol.%)^{7,8,10,11,37,38,40}. Therefore, in this context of low initial temperature and low phenocryst
200 content, our results highlight that the characteristic time of crystallisation has a fundamental role on
201 the likelihood of producing an explosive eruption. Indeed, a small $\tau^{(c)}$ is the primary cause for a
202 significant increase of the syn-eruptive crystal fraction over short timescales during magma ascent,
203 which consequently increases magma viscosity and, thus, the probability of magma fragmentation
204 (Fig. 4f). Moreover, our sensitivity analysis demonstrates that when the syn-eruptive crystal content
205 exceeds 30 vol.%, all numerical solutions reach the fragmentation threshold (Fig. 4f). Indeed, in a
206 fast ascending magma (from our sensitivity analyses we have an average ascent rate between ~5-50
207 m/s), this increase in syn-eruptive crystal content produces a rapid and dramatic increase of
208 viscosity (about one order of magnitude in less than 10 s close to the fragmentation depth),
209 increasing the likelihood of magma fragmentation. Numerical results also show that, as soon as
210 viscosity exceeds 10⁵ Pa s, all the numerical solutions reach the fragmentation threshold, generating
211 an explosive eruption (Fig 4g). Indeed, for a fast ascending magma where outgassing can be
212 neglected and strain-rates are high, the key parameter controlling the triggering of fragmentation is
213 viscosity. Therefore, 10⁵ Pa s represents a minimum viscosity determining a drastic change in
214 eruptive style for activities characterised by high mass eruption rates. This minimum viscosity is
215 one order of magnitude lower than previously reported for low-viscosity magmas^{1,42}.

216 Experimental and natural observations combined with a numerical model allow us to conclude
217 that pre-eruptive temperatures <1100 °C favour the formation of highly explosive basaltic
218 eruptions, such as Plinian volcanism, driven by fast syn-eruptive crystal growth under high
219 undercooling. This implies that all basaltic systems on Earth have the potential to produce powerful
220 explosive eruptions.

221 **METHODS**

222 **Starting material.** The starting material, used for our crystallisation experiments, is a
223 trachybasalt from the lower vents of the 2001 Mt. Etna eruption^{36,43}. The anhydrous, glassy starting
224 material was obtained by melting crushed rock samples in a Pt crucible. Melting was performed in a
225 Nabertherm® MoSi₂ box furnace at 1400 °C and at atmospheric pressure. The melt was left in the
226 furnace for four hours to allow the melt to fully degas and to dissolve the crystals present. The melt
227 was then quenched in air to glass. This procedure was repeated two times to homogenise the melt.
228 Finally, anhydrous glassy cylinders 3 mm in diameter and 4 mm in length were drilled from the
229 synthesized glass for *ex situ* and *in situ* 4D crystallisation experiments.

230 The chemical composition of the anhydrous glassy starting material has been analysed with a
231 Jeol JXA 8530 F microprobe at the Photon Science Institute, University of Manchester, Manchester,
232 UK, and are reported in Supplementary Table 1. Analyses were performed using a 15 kV
233 accelerating voltage, 10 nA beam current and beam size of 10 µm. Standards used for calibration
234 were albite for Na, periclase for Mg, corundum for Al, fayalite for Fe, tephroite for Mn, apatite for
235 P, sanidine for K, wollastonite for Ca and Si and rutile for Ti. Sodium and potassium were
236 measured first to minimize loss owing to volatilisation.

237 Hydrous trachybasaltic glass with ~3 wt. % of H₂O was obtained melting the starting material
238 and homogenizing H₂O in a Pt capsule at 100 MPa and 1200 °C. The hydrous starting glasses were
239 produced using a TZM cold seal pressure vessel apparatus at the School of Earth Sciences,
240 University of Bristol, Bristol, UK. Before to perform crystallisation experiments Raman spectra
241 were collected from the hydrous starting glass, using a Thermo Scientific™ DXRTMxi Raman
242 Imaging Microscope at the School of Earth Sciences, University of Bristol (Bristol, UK) in order to
243 check that the amount of H₂O was ~3 wt. %.

244

245 ***Ex situ* decompression and cooling experiments.**

246 *Ex situ* experiments were performed in order to investigate the process of fast crystallisation in a
247 hydrous trachybasaltic melt during a continuous decompression (0.2 MPa s^{-1}) and cooling ($0.2 \text{ }^\circ\text{Cs}^{-1}$)
248 ¹), simulating magma ascent in the conduit. Two experiments were performed using a TZM cold
249 seal pressure vessel apparatus at the School of Earth Sciences, University of Bristol, Bristol, UK.
250 The redox condition of the apparatus was NNO, adding ~1 vol.% of hydrogen to the pressuring
251 argon. Capsules ($\text{Au}_{80}\text{-Pd}_{20}$) were loaded with hydrous glass with a cylindrical shape. The
252 experimental approach consisted of holding the sample for 30 minutes at 75 MPa and 1070 °C
253 before being decompressed and cooled. The first experiment was quenched after 30 minutes at 75
254 MPa and 1070 °C, in order to texturally characterise the initial conditions before that fast
255 decompression and cooling were applied. In the second experiment, after 30 minutes pressure and
256 temperature were released continuously in 300 s at 0.2 MPa s^{-1} and $0.2 \text{ }^\circ\text{Cs}^{-1}$ respectively, reaching
257 15 MPa and 1010 °C (Supplementary Table 3; Supplementary Fig. 6). The sample was rapidly
258 quenched at the final conditions. Final pressure was chosen as approximate fragmentation pressures
259 calculated by modeling. Decompression and cooling rates were predicted from the conduit model
260 for magma ascent during basaltic Plinian eruptions.

261

262 ***In situ* synchrotron X-ray microtomography experiments.** The experiments were performed
263 at the beamline I12-JEEP⁴⁴, Diamond Light Source, Harwell, UK. For these *in situ* crystallisation
264 experiments, we used the high-temperature resistance Alice furnace⁴⁵, which allows us to control
265 cooling at $0.05 \text{ }^\circ\text{Cs}^{-1}$ to $0.4 \text{ }^\circ\text{Cs}^{-1}$, and the P2R *in situ* rig³⁵ for high speed rotation. Temperature was
266 measured with a R type thermocouple, which was close to the sample, positioned in the middle of
267 the hot spot. The dimension of the Alice furnace's hot spot with homogeneous temperature is
268 ~5x5x5 mm; our samples were positioned within this area. The R type thermocouple provided us
269 the temperature of the sample with an uncertainty of $\pm 5 \text{ }^\circ\text{C}$. The sample holder was an alumina
270 crucible (Supplementary Fig. 2), which is suitable for the temperature range investigated and it has
271 low X-ray attenuation coefficient. The glassy cylinders were heated *in situ* in the Alice furnace up

272 to 1250 °C for 30 minutes (Supplementary Figure 1). After the initial annealing period,
273 crystallisation was induced by decreasing temperature from 1250 °C to 1170 °C or 1150 °C at
274 ambient pressure, holding at the final temperature for 4 h³⁶ (Supplementary Figure 1). After this
275 step, the system was perturbed by a rapid cooling at rate of 0.4 °Cs⁻¹ in order to investigate the rapid
276 crystallisation in real time (Supplementary Figure 1), reaching high undercooling (up to ~180 °C) in
277 a short time.

278 The experiments were performed in phase-contrast mode, setting the sample-to-detector distance
279 at 2300 mm in order to work in the edge-detection regime⁴⁶ (Supplementary Table 4). The
280 projections were acquired using a monochromatic X-ray beam with energy of 53 keV. In each scan,
281 1800 tomographic projections were acquired by the detector with equiangular steps over a full
282 rotation angle of 180° (Supplementary Table 4). The exposure time for the acquisition of each
283 projection was 0.05 s (Supplementary Table 4), therefore, the temporal resolution of each scan was
284 of 90 seconds. The isotropic pixel size is 3.2 µm. The detector was a high-resolution imaging PCO
285 edge camera with optical module 3, corresponding to a field of view of 8.0 mm × 7.0 mm. Scan
286 acquisition started before the end of the annealing, covering the cooling period between 1250 °C
287 and the dwell temperatures (1170 and 1150 °C), the entire duration of the dwell time and the final
288 rapid cooling rate of 0.4 °Cs⁻¹.

289

290 **Image reconstruction and processing.** Tomographic projections were reconstructed into 32-bit
291 slices by using Diamond I12 in-house python codes, using the *gridrec* algorithm^{47,48}
292 ([http://confluence.diamond.ac.uk/display/I12Tech/Reconstruction+](http://confluence.diamond.ac.uk/display/I12Tech/Reconstruction+scripts+for+time+series+tomography)
293 [scripts+for+time+series+tomography](http://confluence.diamond.ac.uk/display/I12Tech/Reconstruction+scripts+for+time+series+tomography))^{49,50}. The pre-processing pipeline includes centre of rotation
294 calculation⁴⁹, zinger removal, blob removal⁵⁰, and regularisation-based ring removal⁵¹.

295 The reconstructed slices were converted to 8-bit raw format and stacked using ImageJ software⁵²
296 to obtain volumes in which the isotropic voxel has an edge size of 3.2 µm. Reconstructed volumes
297 of experiments ET1150 and ET1170 were then cropped using Avizo® software v.8.0 (FEI

298 Visualization Sciences Group) in order to select the volume of interest (VOI) (Supplementary Table
299 4). In the experiment ET1150 plagioclase and pyroxene crystals nucleated and grew in a relatively
300 large pocket of melt (Figs 1 and 2). Therefore, the VOI selected consists of a volume of melt where
301 the rapid crystallisation of plagioclase and pyroxene occurred during the final rapid cooling rate of
302 $0.4\text{ }^{\circ}\text{Cs}^{-1}$. In the experiment ET1170 plagioclase and pyroxene crystals formed in narrow layers of
303 melt (Supplementary Fig. 3), during rapid continuous cooling at a rate of $0.4\text{ }^{\circ}\text{Cs}^{-1}$.

304 Three-dimensional visualization (volume rendering) of the reconstructed volumes was obtained
305 using the commercial software VGStudio 3.0 (Volume Graphics), which allowed us to make 3D
306 textural observations of the plagioclase and pyroxene crystal morphologies (Fig. 2). Therefore, the
307 reconstructed volume of each scan allowed us to quantify when and at which range of temperature
308 plagioclase and pyroxene crystals were able to form.

309

310 **Image segmentation and analysis of plagioclase.** Segmentation is the process that allows
311 separation of objects from the background to obtain binary volumes containing only the feature of
312 interest. Segmentation of plagioclase crystals from the glassy matrix was performed using the semi-
313 automatic volume segmentation^{53,54} in Avizo software v. 8.0 (Supplementary Table 4). This
314 segmentation requires manual drawing of the outlines of crystals on the 2D slices. This is repeated
315 every 5–10 slices, depending on the size of the crystal and the complexity of their shape, along the
316 crystal length. The crystal shape is reconstructed automatically by the software through an
317 interpolation procedure. The advantage of this technique is that the operator can obtain the real
318 morphology of the object of interest by visual inspection^{53,54}.

319 The reconstructed 3D images were processed and analysed with the Pore3D software library,
320 custom-developed at Elettra⁵⁵. The Pore3D software allowed us to quantify the number of
321 plagioclase crystals, the volume and the maximum length of each crystal, operating directly in the
322 3D domain^{55,56}. As we were able to obtain the 3D shape of plagioclase crystals and the real
323 maximum axis length (L_{3D}) we could calculate the growth rate (Y_{L3D}) of plagioclase crystals

324 (Supplementary Table 2), using the experimental duration of growth (experimental duration). The
325 growth rate was estimated using the following equation⁵³:

326
$$Y_{L3D} = (L_{3D} * 0.5) / t_{\text{growth}}$$

327 where t_{growth} is the time required for crystal growth. The microtomography images give us the
328 opportunity to measure the volume of crystals. The volumetric growth rate (Y_V) was calculated
329 (Supplementary Table 2) using the following relationship⁵³:

330
$$Y_V = (V * 0.5) / t_{\text{exp}}$$

331 where V is the volume of the crystal.

332

333 **Image analysis of pyroxene growth kinetics.** Back-scattered electron (BSE) images were
334 collected, using a JEOL JSM-6390LA FE-SEM at the School of Earth and Environmental Sciences,
335 University of Manchester, Manchester, UK, in order to analyse the pyroxene morphologies and
336 kinetics. We used an acceleration voltage of 15 kV and beam current of 10 nA. The sizes of
337 dendritic pyroxene crystals were measured in the 2D domain, using BSE images and ImageJ
338 software⁵², as pyroxene morphologies formed during continuous cooling are difficult to resolve and
339 analyse in the 3D domain. The pyroxene growth rate is calculated by dividing the entire length of
340 the dendritic crystal over the duration of the pyroxene growth (Supplementary Table 2), as dendritic
341 crystals grow in one direction.

342

343 **Electron microprobe analysis.** Samples obtained with *ex situ* and *in situ* crystallisation
344 experiments were analysed with a JEOL JXA-8530F field emission electron microprobe at the
345 Photon Science Institute, University of Manchester, Manchester, UK. For both instruments, the
346 operating conditions were as follows: 15 kV accelerating voltage, 10 nA beam current, and beam
347 diameter of 10 or 5 μm (the latter for microlites). Sodium and potassium were measured first to
348 minimise loss by volatilisation. Calibration standards were albite for Na, periclase for Mg,
349 corundum for Al, fayalite for Fe, tephroite for Mn, apatite for P, sanidine for K, wollastonite for Ca

350 and Si and rutile for Ti. Several compositional maps, with a nominal resolution of 1 μm^2 , have been
351 also collected using the EPMA (EPMA map, are reported in Supplementary Figs. 4, 5 and 7).

352

353 **Constitutive equations for the conduit model.** In this work we use the 1D steady-state model
354 for magma ascent described by ref. (21, 23, 57). The governing equations used in this work are
355 reported in ref. (57). The application to a specific volcano is achieved by providing constitutive
356 equations to describe the specific rheological, solubility, crystallisation, outgassing, and
357 fragmentation behaviour of the system.

358 Following ref. (58), the viscosity of the liquid phase is modelled as:

359
$$\mu_l = \mu_{melt} \cdot \theta(x_c^l),$$

360 where μ_{melt} is the viscosity of the bubble-free, crystal-free liquid phase and θ is a factor which
361 increases viscosity attributed to the presence of crystals⁵⁹.

362 We use an empirical relationship to estimate μ_{melt} as a function of water concentration and
363 temperature, as in ref. (60) (based on the Vogel-Fulcher-Tammann equation):

364
$$\log(\mu_{melt}) = A + \frac{B(y, x_{d_{H_2O}}^{md})}{T - C(y, x_{d_{H_2O}}^{md})},$$

365 where the viscosity μ_{melt} is in Pa s and T is the temperature in Kelvin. The parameter A is the
366 logarithmic value of the viscosity at infinite temperature and it is assumed to be constant for all
367 melts. The parameters B and C, instead, are functions of the melt composition y and of the dissolved
368 water content $x_{d_{H_2O}}^{md}$. In this work, we used the composition of the average melt inclusion
369 composition (Etna 122 B.C.) from ref. (61). Furthermore, as crystallisation proceeds, viscosity is
370 increased according to the empirical model described in ref. (62):

371
$$\theta = \frac{1 + \varphi^\delta}{[1 - F(\varphi, \xi, \gamma)]^{B\phi^*}},$$

372 where

373
$$F = (1 - \xi) \operatorname{erf} \left[\frac{\sqrt{\pi}}{2(1 - \xi)} \varphi (1 + \varphi^\gamma) \right], \quad \varphi = \frac{\left(\sum_{j=1}^{n_c} x_{c_j}^l \right)}{\phi^*}.$$

374 The fitting parameters B, δ, ξ, γ and ϕ^* chosen for this work are the same used in ref. (63).

375 The model proposed in this work takes into account two different gas components: water and
 376 carbon dioxide. The equilibrium profile of the dissolved gas content $x_{d_i}^{md,eq}$ of component i follows
 377 the Henry's Law, i.e.

378
$$x_{d_i}^{md,eq} = \sigma_i \left(\frac{P_{g,i}}{\bar{P}} \right)^{\varepsilon_i},$$

379 where $P_{g,i} = \alpha_{g_i} P_g / \alpha_g$ is the partial pressure of the i -th gas component expressed in Pa, $\bar{P} = 1$
 380 Pa is used to make the expression in the brackets adimensional, σ_i is the solubility coefficient and ε_i
 381 is the solubility exponent. We assume that the solubility parameter σ_i and ε_i are constant during
 382 ascent. For this work we adopted the following parameters $\sigma_{H_2O} = 1.8911 \times 10^{-6}$; $\varepsilon_{H_2O} = 0.5257$;
 383 $\sigma_{CO_2} = 2.2154 \times 10^{-12}$; $\varepsilon_{CO_2} = 1.075$. In this work, we assume also equilibrium exsolution, which
 384 means that the dissolved volatile contents always follow the equilibrium profile.

385 The crystallisation model adopted here has been proposed in ref. (23). We consider the three
 386 different major crystal components erupted by Etna volcano: plagioclase, pyroxene and olivine. We
 387 assume that crystals stay coupled with the melt (i.e. no fractional crystallisation). For a better
 388 modelling of crystal nucleation and growth, we also assume that the equilibrium crystal contents are
 389 functions of temperature, pressure and dissolved water content. With these assumptions, the
 390 equilibrium mass fraction $x_{c_j}^{l,eq}$ of crystal phase j is computed using the polynomial function

391
$$\begin{aligned} x_{c_j}^{l,eq}(P^*, T^*, x_d^*) &= \zeta_{j,1}(P^*)^2 + \zeta_{j,2}(T^*)^2 + \zeta_{j,3}(x_d^*)^2 + \zeta_{j,4}(P^*)(T^*) + \\ &+ \zeta_{j,5}(T^*)(x_d^*) + \zeta_{j,6}(x_d^*)(P^*) + \zeta_{j,7}(P^*) + \zeta_{j,8}(T^*) + \zeta_{j,9}(x_d^*) + \zeta_{j,10}, \end{aligned}$$

392 where P^* is the liquid pressure expressed in bars, T^* is the temperature expressed in Celsius
 393 degrees and x_d^* is the dissolved water concentration in weight percent. From $x_{c_j}^{l,eq}$, the equilibrium
 394 crystal volume fraction β_j^{eq} can be computed using the relation

395
$$\beta_j^{eq} = \frac{\rho_l x_{c_j}^{l,eq}}{\rho_{c_j}}.$$

396 The parameters $\zeta_{j,i}$ are calculated fitting the polynomial function over a large range of data
 397 obtained at different pressures, temperatures and water contents with alphaMELTS⁶⁴, a command
 398 line version of MELTS⁶⁵. As previously, we used the average melt inclusion composition (Etna 122
 399 B.C.) from ref. (61).

400 Disequilibrium crystallisation is considered in our model and characteristic times controls the
 401 time needed to reach equilibrium crystal content. The differential equation in the conduit model
 402 which describes the crystal volume fraction within the conduit is the following²¹:

403
$$\frac{\partial \alpha_l \rho_c \beta u_l}{\partial z} = -\frac{1}{\tau^{(c)}} \alpha_l \rho_c (\beta - \beta^{eq}).$$

404 Here, α_l is the volume fraction of the liquid phase, ρ_c is the density of the crystals, u_l is the
 405 velocity of the liquid phase, z is the vertical axis, β is the actual total crystal volume fraction,
 406 whereas β^{eq} is the equilibrium total crystal volume fraction. If we multiply all the terms by the
 407 characteristic time $\tau^{(c)}$, we notice that the smaller is $\tau^{(c)}$, the smaller has to be $(\beta - \beta^{eq})$. In other
 408 terms, the smaller is the characteristic time, the faster the crystals will reach the equilibrium value.

409 Formally, as described in La Spina et al. (ref. 21), the characteristic time reflects the time
 410 required to reduce the difference between the actual and the equilibrium value to e^{-1} (~37%) of the
 411 initial difference. This means that, if β_0 is the initial value of a physical parameter β (which, in our
 412 case, is the crystal volume fraction), and β_{eq} is the equilibrium value in response to a perturbation of
 413 the system, at the characteristic time τ , we have

414
$$\beta(\tau) = \beta^{eq} + e^{-1}(\beta_0 - \beta^{eq}).$$

415 The experimental phase diagram for Etna basalt erupted during the 122 B.C. eruption³⁷ provides
 416 the plagioclase and pyroxene liquidus at different pressures and temperatures, whilst the conduit
 417 model is able to track temperature evolution within the conduit. Combining both of these data, we
 418 can estimate ΔT with respect to the plagioclase and pyroxene liquidus during magma ascent.

419 For this work, as we are interested in the highly explosive activity, we assumed no relative
420 velocity between gas and melt. Furthermore, as we indicated in the main text, we used as
421 fragmentation model the strain-rate criterion introduced by ref. (1).

422

423 **Initial condition for the sensitivity analysis.**

424 The range of input parameters adopted for the sensitivity analysis are the following: 140–160
425 MPa for the inlet pressure at 6000 m depth, 1050–1100 °C for the magma inlet temperature, 5–30 m
426 for the radius of the conduit, 2.0–4.0 wt.% for the total water content, 0.1–2.0 wt.% for the total
427 CO₂ content, 0–20 vol.% for the initial phenocrysts, and 1–1000 s for the characteristic time of
428 crystallisation. As we do not know the probability distribution of the uncertain input parameters,
429 we have assumed a uniform distribution within the aforementioned ranges. The sensitivity analysis
430 was performed on using the DAKOTA toolkit (Design Analysis Kit for Optimization and Terascale
431 Applications)⁶⁶, an open-source software developed at Sandia National Laboratories that provides a
432 flexible and extensible interface between analysis codes and iterative systems analysis methods
433 such as uncertainty quantification, sensitivity analysis, optimization, and parameter estimation.

434 **References**

435 1. Papale, P. Strain-induced magma fragmentation in explosive eruptions. *Nature* **397**, 425
436 (1999).

437 2. Dingwell, D. B. (1996). Volcanic Dilemma--Flow or Blow?. *Science*, 273(5278), 1054-1055.

438 3. Carey, S., & Sigurdsson, H. (1989). The intensity of plinian eruptions. *Bulletin of*
439 *Volcanology*, 51(1), 28-40.

440 4. Wilson, L. (1976). Explosive volcanic eruptions—III. Plinian eruption columns. *Geophysical*
441 *Journal International*, 45(3), 543-556.

442 5. Polacci, M., Corsaro, R. A. & Andronico, D. Coupled textural and compositional
443 characterization of basaltic scoria: Insights into the transition from Strombolian to fire fountain
444 activity at Mount Etna, Italy. *Geology* **34**, 201-204 (2006).

445 6. Coltelli, M., Del Carlo, P. & Vezzoli, L. Discovery of a Plinian basaltic eruption of Roman
446 age at Etna volcano, Italy. *Geology* **26**, 1095-1098 (1998).

447 7. Houghton, B. F., Wilson, C. J. N., Del Carlo, P., Coltelli, M., Sable, J. E. & Carey, R. The
448 influence of conduit processes on changes in style of basaltic Plinian eruptions: Tarawera 1886 and
449 Etna 122 BC. *Journal of Volcanology and Geothermal Research* **137**, 1-14 (2004).

450 8. Sable, J. E., Houghton, B. F., Del Carlo, P. & Coltelli, M. Changing conditions of magma
451 ascent and fragmentation during the Etna 122 BC basaltic Plinian eruption: Evidence from clast
452 microtextures. *Journal of Volcanology and Geothermal Research* **158**, 333-354 (2006).

453 9. Houghton, B. F. & Gonnermann, H. M. Basaltic explosive volcanism: constraints from
454 deposits and models. *Chemie der Erde-Geochemistry* **68**, 117-140 (2008).

455 10. Sable, J. E. Houghton, B. F., Wilson, C. J. N. & Carey, R. J. Eruption mechanisms during the
456 climax of the Tarawera 1886 basaltic Plinian eruption inferred from microtextural characteristics of
457 the deposits. *Studies in Volcanology: The Legacy of George Walker. Special Publications of*
458 *IAVCEI* **2**, 129-154 (2009).

- 459 11. Costantini, L., Houghton, B. F. & Bonadonna, C. Constraints on eruption dynamics of
460 basaltic explosive activity derived from chemical and microtextural study: the example of the
461 Fontana Lapilli Plinian eruption, Nicaragua. *Journal of Volcanology and Geothermal Research* **189**,
462 207-224 (2010).
- 463 12. Melnik, O., & Sparks, R. S. J. (1999). Nonlinear dynamics of lava dome extrusion. *Nature*,
464 402(6757), 37.
- 465 13. Gonnermann, H. M., & Manga, M. (2003). Explosive volcanism may not be an inevitable
466 consequence of magma fragmentation. *Nature*, 426(6965), 432.
- 467 14. Gonnermann, H. M. (2015). Magma fragmentation. *Annual Review of Earth and Planetary*
468 *Sciences*, 43, 431-458.
- 469 15. Alidibirov, M., & Dingwell, D. B. (1996). Magma fragmentation by rapid decompression.
470 *Nature*, 380(6570), 146.
- 471 16. Zhang, Y. (1999). A criterion for the fragmentation of bubbly magma based on brittle failure
472 theory. *Nature*, 402(6762), 648.
- 473 17. Spieler, O., Kennedy, B., Kueppers, U., Dingwell, D. B., Scheu, B., & Taddeucci, J. (2004).
474 The fragmentation threshold of pyroclastic rocks. *Earth and Planetary Science Letters*, 226(1-2),
475 139-148.
- 476 18. Kueppers, U., Scheu, B., Spieler, O., & Dingwell, D. B. (2006). Fragmentation efficiency of
477 explosive volcanic eruptions: A study of experimentally generated pyroclasts. *Journal of*
478 *Volcanology and Geothermal Research*, 153(1-2), 125-135.
- 479 19. Giordano, D. & Dingwell, D. Viscosity of hydrous Etna basalt: implications for Plinian-style
480 basaltic eruptions. *Bulletin of Volcanology* **65**, 8-14 (2003).
- 481 20. Moitra, P., Gonnermann, H. M., Houghton, B. F. & Tiwary, C. S. Fragmentation and Plinian
482 eruption of crystallizing basaltic magma. *Earth and Planetary Science Letters* **500**, 97-104 (2018).

- 483 21. La Spina, G., Burton, M., Vitturi, M. D. M. & Arzilli, F. Role of syn-eruptive plagioclase
484 disequilibrium crystallisation in basaltic magma ascent dynamics. *Nature communications* **7**, 13402
485 (2016).
- 486 22. Cashman, K. & Blundy, J. Degassing and crystallisation of ascending andesite and
487 dacite. *Philosophical Transactions of the Royal Society of London A: Mathematical, Physical and*
488 *Engineering Sciences* **358**, 1487-1513 (2000).
- 489 23. La Spina, G., Burton, M., de' Michieli Vitturi, M. Temperature evolution during magma
490 ascent in basaltic effusive eruptions: a numerical application to Stromboli volcano. *Earth Planet.*
491 *Sci. Lett.* **426**, 89–100 (2015).
- 492 24. Hammer, J. E. & Rutherford, M. J. An experimental study of the kinetics of decompression-
493 induced crystallization in silicic melt. *Journal of Geophysical Research: Solid Earth* **107**, ECV-8
494 (2002).
- 495 25. Couch, S., Harford, C. L., Sparks, R. S. J. & Carroll, M. R. Experimental constraints on the
496 conditions of formation of highly calcic plagioclase microlites at the Soufriere Hills Volcano,
497 Montserrat. *Journal of Petrology* **44**, 1455-1475 (2003).
- 498 26. Shea, T. & Hammer, J. E. Kinetics of cooling-and decompression-induced crystallization in
499 hydrous mafic-intermediate magmas. *Journal of Volcanology and Geothermal research* **260**, 127-
500 145 (2013).
- 501 27. Agostini, C., Fortunati, A., Arzilli, F., Landi, P. & Carroll, M. R. Kinetics of crystal
502 evolution as a probe to magmatism at Stromboli (Aeolian Archipelago, Italy). *Geochimica et*
503 *cosmochimica acta* **110**, 135-151 (2013).
- 504 28. Vona, A. & Romano, C. The effects of undercooling and deformation rates on the
505 crystallization kinetics of Stromboli and Etna basalts. *Contributions to Mineralogy and*
506 *Petrology* **166**, 491-509 (2013).

- 507 29. Kolzenburg, S., Giordano, D., Hess, K. U. & Dingwell, D. B. Shear Rate-Dependent
508 Disequilibrium Rheology and Dynamics of Basalt Solidification. *Geophysical Research Letters* **45**,
509 6466-6475 (2018).
- 510 30. Marsh, B. D. (1998). On the interpretation of crystal size distributions in magmatic
511 systems. *Journal of Petrology*, *39*(4), 553-599.
- 512 31. Cashman, K. V. Relationship between plagioclase crystallization and cooling rate in basaltic
513 melts. *Contributions to Mineralogy and Petrology* **113**, 126-142 (1993).
- 514 32. Conte, A. M., Perinelli, C. & Trigila, R. Cooling kinetics experiments on different Stromboli
515 lavas: Effects on crystal morphologies and phases composition. *Journal of Volcanology and*
516 *Geothermal Research* **155**, 179-200 (2006).
- 517 33. Szramek, L., Gardner, J. E. & Hort, M. Cooling-induced crystallization of microlite crystals
518 in two basaltic pumice clasts. *American Mineralogist* **95**, 503-509 (2010).
- 519 34. Brugger, C. R. & Hammer, J. E. Crystallization kinetics in continuous decompression
520 experiments: implications for interpreting natural magma ascent processes. *Journal of Petrology* **51**,
521 1941-1965 (2010).
- 522 35. Karagadde, S., Lee, P. D., Cai, B., Fife, J. L., Azeem, M. A., Kareh, K. M., Puncreobutr, C.,
523 Tsivoulas, D., Connolley, T. & Atwood, R. C. Transgranular liquation cracking of grains in the
524 semi-solid state. *Nature communications* **6**, 8300 (2015).
- 525 36. Polacci, M., Arzilli, F., La Spina, G., Le Gall, N., Cai, B., Hartley, M. E., Di Genova, D., Vo,
526 N. T., Nonni, S., Atwood, R. C., Llewellyn, E. W., Lee, P. D. & Burton, M. R. Crystallisation in
527 basaltic magmas revealed via in situ 4D synchrotron X-ray microtomography. *Scientific Reports* **8**,
528 8377 (2018).
- 529 37. Goepfert, K. & Gardner, J. E. Influence of pre-eruptive storage conditions and volatile
530 contents on explosive Plinian style eruptions of basic magma. *Bulletin of Volcanology* **72**, 511-521
531 (2010).

- 532 38. Szramek, L. A. Mafic Plinian eruptions: Is fast ascent required? *Journal of Geophysical*
533 *Research: Solid Earth* **121**, 7119-7136 (2016).
- 534 39. Suzuki, Y. & Fujii, T. Effect of syneruptive decompression path on shifting intensity in
535 basaltic sub-Plinian eruption: Implication of microlites in Yufune-2 scoria from Fuji volcano, Japan.
536 *Journal of Volcanology and Geothermal Research*, **198**, 158-176 (2010).
- 537 40. Campagnola, S., Romano, C., Mastin, L. G. & Vona, A. Confort 15 model of conduit
538 dynamics: applications to Pantelleria Green Tuff and Etna 122 BC eruptions. *Contributions to*
539 *Mineralogy and Petrology* **171**, 60 (2016).
- 540 41. Cassidy, M., Manga, M., Cashman, K., & Bachmann, O. (2018). Controls on explosive-
541 effusive volcanic eruption styles. *Nature communications*, 9, 2839.
- 542 42. Namiki, A. & Manga, M. Transition between fragmentation and permeable outgassing of low
543 viscosity magmas. *Journal of Volcanology and Geothermal Research* **169**, 48-60 (2008).
- 544
- 545
- 546 43. Corsaro, R. A., Miraglia, L. & Pompilio, M. Petrologic evidence of a complex plumbing
547 system feeding the July-August 2001 eruption of Mt. Etna, Sicily, Italy. *B. Volcanol.* **69**, 401–421
548 (2007).
- 549 44. Drakopoulos, M., Connolley, T., Reinhard, C., Atwood, R., Magdysyuk, O., Vo, N., Hart,
550 M., Connor, L., Humphreys, B., Howell, G. & Davies, S. I12: the joint engineering, environment
551 and processing (JEEP) beamline at diamond light source. *Journal of synchrotron radiation* **22**, 828-
552 838 (2015).
- 553 45. Azeem, M. A., Lee, P. D., Phillion, A. B., Karagadde, S., Rockett, P., Atwood, R. C.,
554 Courtois, L., Rahman, K. M. & Dye, D. Revealing dendritic pattern formation in Ni, Fe and Co
555 alloys using synchrotron tomography. *Acta Materialia* **128**, 241-248 (2017).
- 556 46. Cloetens, P., Barrett, R., Baruchel, J., Guigay, J. P. & Schlenker, M. Phase objects in syn-
557 chrotron radiation hard X-ray imaging. *J. Phys. D. Appl. Phys.* **29**, 133–46 (1996).

- 558 47. O'sullivan, J. D. A fast sinc function gridding algorithm for Fourier inversion in computer
559 tomography. *IEEE transactions on medical imaging* **4**, 200-207 (1985).
- 560 48. Gürsoy, D., De Carlo, F., Xiao, X. & Jacobsen, C. TomoPy: a framework for the analysis of
561 synchrotron tomographic data. *Journal of synchrotron radiation* **21**, 1188-1193 (2014).
- 562 49. Vo, N. T., Drakopoulos, M., Atwood, R. C. & Reinhard, C. Reliable method for calculating
563 the center of rotation in parallel-beam tomography. *Opt. Express* **22**, 19078–19086 (2014).
- 564 50. Vo, N. T., Atwood, R. C. and Drakopoulos, M. Superior techniques for eliminating ring
565 artifacts in X-ray micro-tomography. *Optics express* **26**, 28396-28412 (2018).
- 566 51. Titarenko, S., Withers, P. J. & Yagola, A. An analytical formula for ring artefact suppression
567 in X-ray tomography. *Applied Mathematics Letters* **23**, 1489-1495 (2010).
- 568 52. Abramoff M. D., Magalhaes P. J., Ram S. J. Image processing with ImageJ. *Biophot. Int.* **11**,
569 36–42 (2004).
- 570 53. Arzilli, F., Mancini, L., Voltolini, M., Cicconi, M. R., Mohammadi, S., Giuli, G., Mainprice,
571 D., Paris, E., Barou, F. & Carroll, M. R. Near-liquidus growth of feldspar spherulites in trachytic
572 melts: 3D morphologies and implications in crystallization mechanisms. *Lithos* **216**, 93-105 (2015).
- 573 54. Arzilli, F., Polacci, M., Landi, P., Giordano, D., Baker, D. R. & Mancini, L. A novel protocol
574 for resolving feldspar crystals in synchrotron X-ray microtomographic images of crystallized
575 natural magmas and synthetic analogs. *American Mineralogist* **101**, 2301-2311 (2016).
- 576 55. Brun, F., Mancini, L., Kasae, P., Favretto, S., Dreossi, D. & Tromba, G. Pore3D: a software
577 library for quantitative analysis of porous media. *Nucl. Instrum. Meth. A* **615**, 326–332 (2010).
- 578 56. Ohser, J. & Mücklich, F. Statistical analysis of microstructure in material science. Barnett V,
579 editor. *Statistics in Practice*, West Sussex, England: John Wiley & Sons; (2000).
- 580 57. La Spina, G., Polacci, M., Burton, M. & de' Michieli Vitturi, M. Numerical investigation of
581 permeability models for low viscosity magmas: application to the 2007 Stromboli effusive eruption
582 *Earth and Planetary Science Letters* **473**, 279-290 (2017).

- 583 58. de' Michieli Vitturi, M., Clarke, A. B., Neri, A. & Voight, B. Transient effects of magma
584 ascent dynamics along a geometrically variable dome-feeding conduit. *Earth Planet. Sci. Lett.* **295**,
585 541–553 (2010).
- 586 59. Caricchi, L., Burlini, L., Ulmer, P., Gerya, T., Vassalli, M. & Papale, P. Non-Newtonian
587 rheology of crystal-bearing magmas and implications for magma ascent dynamics. *Earth Planet.*
588 *Sci. Lett.* **264**, 402–419 (2007).
- 589 60. Giordano, D., Russell, J. K. & Dingwell, D. B. Viscosity of magmatic liquids: a model. *Earth*
590 *Planet. Sci. Lett.* **271**, 123–134 (2008).
- 591 61. Del Carlo, P. & Pompilio, M. The relationship between volatile content and the eruptive style
592 of basaltic magma: the Etna case. *Annals of Geophysics*, **47** (2004).
- 593 62. Costa, A., Caricchi, L. & Bagdassarov, N. A model for the rheology of particle-bearing
594 suspensions and partially molten rocks. *Geochem. Geophys. Geosyst.* **10**, (2009).
- 595 63. Vona, A., Romano, C., Dingwell, D. & Giordano, D. The rheology of crystal-bearing basaltic
596 magmas from Stromboli and Etna. *Geochim. Cosmochim. Acta* **75**, 3214–3236 (2011).
- 597 64. Smith, P. M. & Asimow, P. D. Adibat_1ph: a new public front-end to the MELTS,
598 pMELTS, and pHMELTS models. *Geochem. Geophys. Geosyst.* **6**, (2005).
- 599 65. Ghiorso, M. S. & Sack, R. O. Chemical mass transfer in magmatic processes IV. A revised
600 and internally consistent thermodynamic model for the interpolation and extrapolation of liquid–
601 solid equilibria in magmatic systems at elevated temperatures and pressures. *Contrib. Mineral.*
602 *Petrol.* **119**, 197–212 (1995).
- 603 66. Adams, B. M., Ebeida, M. S., Eldred, M. S., Geraci, G., Jakeman, J. D., Maupin, K. A.,
604 Monschke, J. A., Swiler, L. P., Stephens, J. A., Vigil, D. M., Wildey, T. M., Bohnhoff, W. J.,
605 Dalbey, K. R., Eddy, J. P., Frye, J. R., Hooper, R. W., Hu, K. T., Hough, P. D., Khalil, M.,
606 Ridgway, E. M. & Rushdi, A. DAKOTA, A Multilevel Parallel Object-Oriented Framework for
607 Design Optimization, Parameter Estimation, Uncertainty Quantification, and Sensitivity Analysis
608 Version 6.6 User's Manual Tech. rep., SAND2014-4633, Tech. rep., SAND2014-4633, (2017).

609

610

611 **Supplementary information** is available in the online version of the paper.

612

613 **Acknowledgements**

614 The research leading to these results has received funding from the RCUK NERC DisEqm
615 project (NE/N018575/1) and (NE/M013561/1). The beamtime on I12 was provided by Diamond
616 Light Source (EE16188-1) and laboratory space by the Research Complex at Harwell.

617

618 **Author Contributions**

619 M.P., F.A., M.R.B., and P.D.L. conceived the research project. F.A., M.P., G.L.S., N.L.G., B.C.,
620 M.E.H., D.D.G., N.T.V., S.N., R.C.A., E.W.L., P.D.L. and M.R.B. contributed to the beamline
621 experiments. F.A. collected the volcanic rocks for the starting material. D.D.G., H.M and R.A.B.
622 prepared the starting material. F.A., M.P. and G.L.S performed image reconstruction. F.A. and M.P.
623 performed image processing. F.A. performed image segmentation and analysis. G.L.S. performed
624 simulations using the conduit model. R.A.B. and F.A. performed ex situ decompression
625 experiments. E.C.B., F.A. and G.L.S. collected samples of the Etna 122 BC Plinian eruption. E.C.B.
626 and F.A. acquired and analysed back-scattered electron images of Etna Plinian eruption's samples.
627 F.A., G.L.S., M.R.B., M.P. and E.C.B. wrote the manuscript, with contributions from all other
628 authors.

629

630 **Author Information**

631 Reprints and permissions information is available at www.nature.com/reprints. The authors
632 declare no competing financial interests. Readers are welcome to comment on the online version of
633 the paper. Correspondence and requests for materials should be addressed to F.A.
634 (fabio.arzilli@manchester.ac.uk)

635

636

637

638 **FIGURES**

639 Figure 1. Crystallisation through time. Reconstructed axial slices during continuous cooling at
640 $0.4\text{ }^{\circ}\text{C s}^{-1}$: (a) frame after 24 s from the onset of the cooling, in which the temperature ranges
641 between 1144 and 1112 $^{\circ}\text{C}$ (average 1128 $^{\circ}\text{C}$); (b) frame after 208 s, in which the temperature
642 ranges between 1073 and 1034 $^{\circ}\text{C}$ (average 1054 $^{\circ}\text{C}$); (c) frame after 392 s, in which the
643 temperature ranges between 997 and 959 $^{\circ}\text{C}$ (average 978 $^{\circ}\text{C}$). m = melt; plg = plagioclase; px =
644 pyroxene.

645

646 Figure 2. Plagioclase crystal morphology. (a) The 3D volume rendering of sample SS1150 shows
647 the morphology and the spatial distribution of plagioclase crystals that formed during the rapid
648 cooling at $96 < \Delta T < 155\text{ }^{\circ}\text{C}$. (b) 3D view of the plagioclase with swallow-tailed crystal morphology.
649 (c) Back scattered electron image of plagioclase with swallow-tailed crystal morphology. (d) Back
650 scattered electron image of plagioclase with swallow-tailed crystal morphology produced during the
651 Etna 122 B.C Plinian eruption. Note heterogeneous nucleation of pyroxene around plagioclase, seen
652 as a light-coloured halo, and similar to that seen in figure 1b.

653

654 Figure 3. Model results during magma ascent. (a) Undercooling as a function of depth, calculated
655 for $\tau(c) = 10$ (blue) and 1000 s (red). Cooling is driven by adiabatic expansion of gas, mitigated by
656 latent heat of crystallisation particularly in the fast crystallising case. (b) Crystal content in vol%,
657 demonstrating the rapid increase in crystal load when $\tau(c) = 10$ s. (c) Magma viscosity,
658 demonstrating that the higher crystal load produces 3-4 order of magnitude increase in viscosity,
659 leading to fragmentation.

660

661 Figure 4. Relationships between characteristic time, initial temperature, initial H₂O content of the
662 magma, syn-eruptive crystal content and magma viscosity and the undercooling of the system at the
663 fragmentation level. These figures were calculated using repeated runs of the model while changing
664 individual parameters to reveal the sensitivity of the system to each parameter. Likelihood of
665 explosive eruption as a function of a specific parameter arises from the ratio between the number of
666 model runs producing explosive eruptions divided by the total number of model runs used to test
667 that parameter. Therefore, this is not a probabilistic assessment of eruption risk, but instead depends
668 on the critical model parameters, which control when fragmentation occurs, and the calculated
669 probabilities depend on the choice of upper and lower limits chosen for each investigated
670 parameter. (a) Sobol index. (b) Undercooling vs magma temperature before ascent. (c)
671 Undercooling vs the initial H₂O content of the magma (dissolved and exsolved). For a given input
672 value, the solid lines are the mean of a given output parameter obtained from all the simulations
673 assuming that input value. The error bars, instead, represent the spread of that output values with
674 respect to the corresponding mean. (d) Frequency of explosive eruptions vs magma temperature
675 before ascent. (e) Explosion frequency vs initial phenocryst content. (f) Frequency of explosive
676 eruptions vs syn-eruptive crystal content at the fragmentation level. (g) Frequency of explosive
677 eruptions vs magma viscosity at the fragmentation level.

678

679

680

681

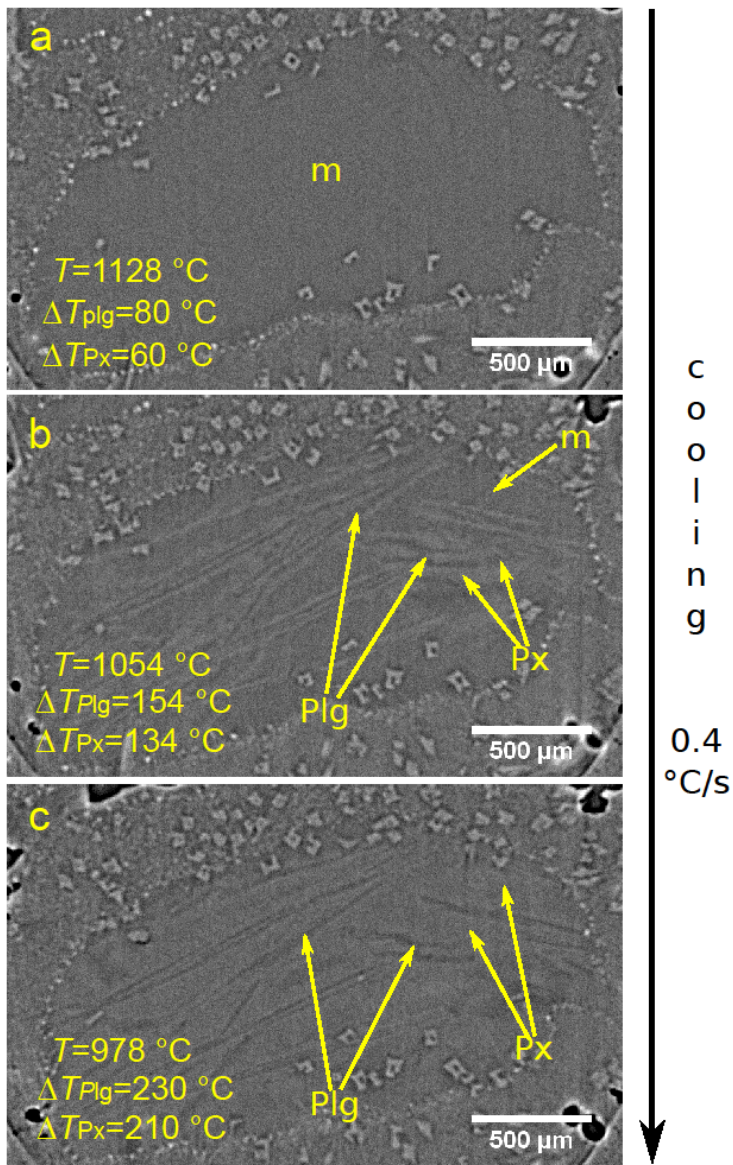
682

683

684

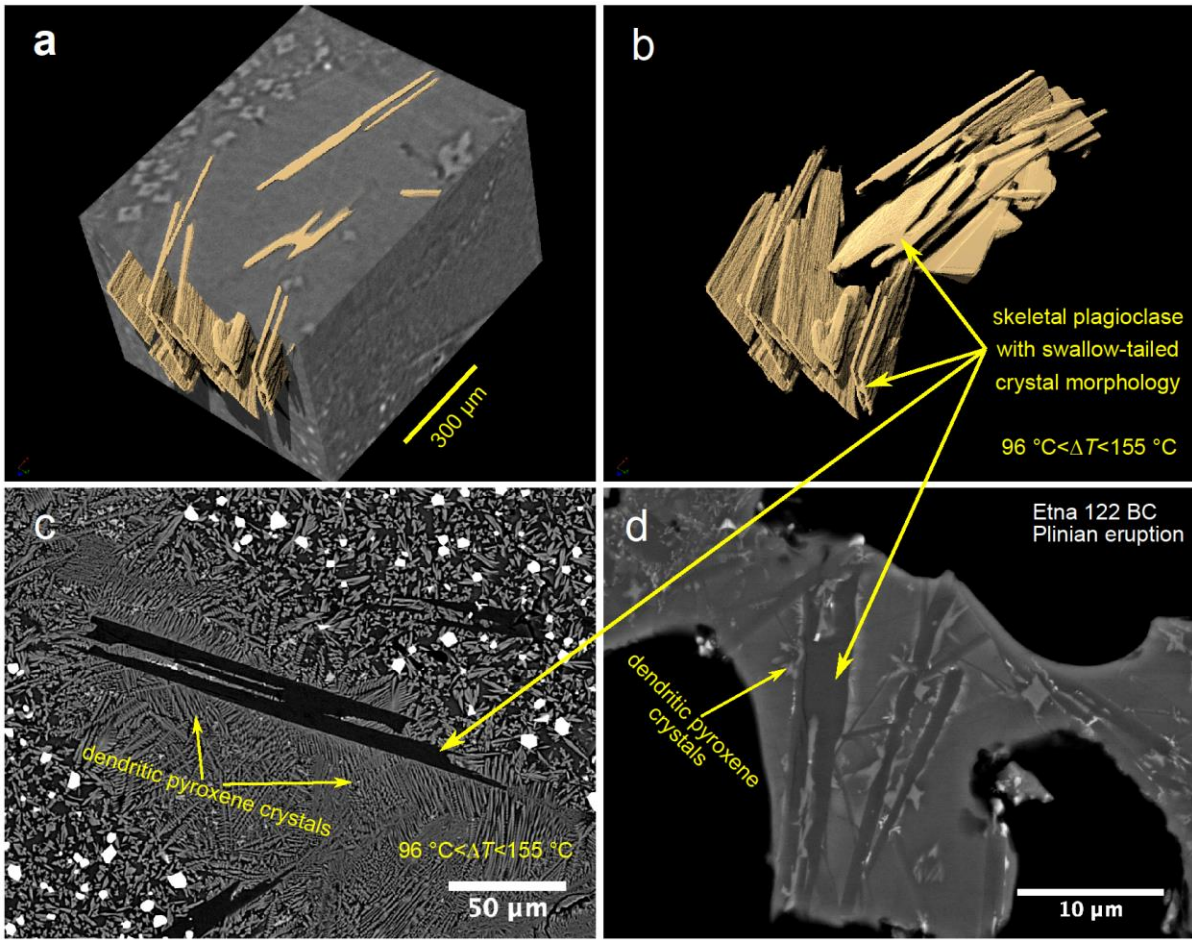
685

686



687

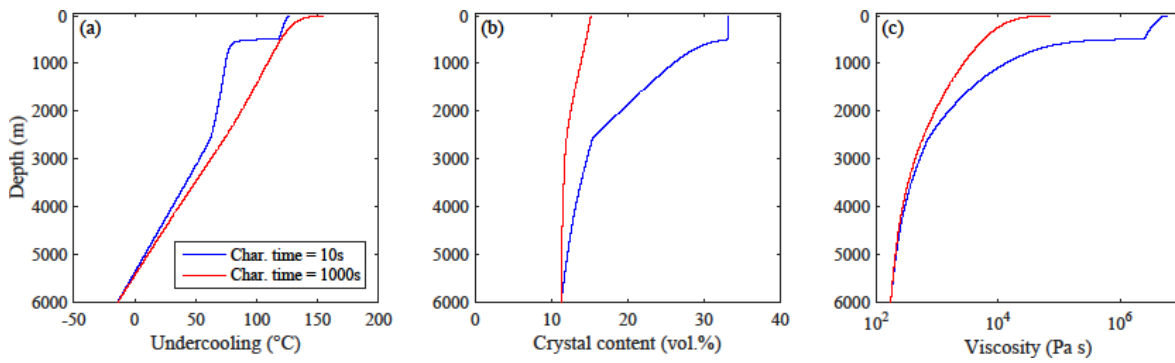
Figure 1



688

689 Figure 2

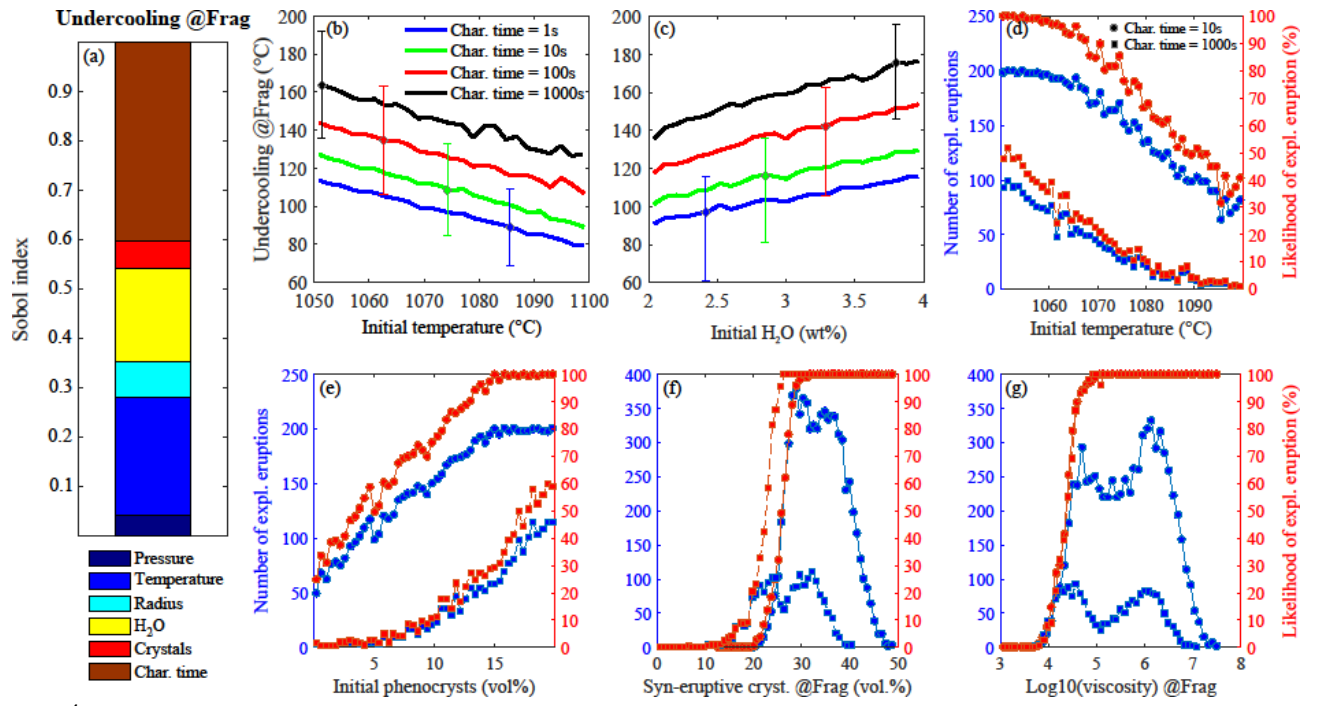
690



691

692 Figure 3

693



694
695 Figure 4

696